PLOS ONE

RESEARCH ARTICLE

Comparison of Texture Features Derived from Static and Respiratory-Gated PET Images in Non-Small Cell Lung Cancer

Stephen Yip[1]*, Keisha McCall[2], Michalis Aristophanous[3], Aileen B. Chen[1], Hugo J. W. L. Aerts[1,4☯], Ross Berbeco[1☯]

1. Department of Radiation Oncology, Brigham and Women's Hospital, Dana-Farber Cancer Institute and Harvard Medical School, Boston, Massachusetts, United States of America, **2.** Department of Radiology, Dana-Farber Cancer Institute and Harvard Medical School, Boston, Massachusetts, United States of America, **3.** Department of Radiation Physics, Division of Radiation Oncology, University of Texas MD Anderson Cancer Center, Houston, Texas, United States of America, **4.** Department of Radiology, Brigham and Women's Hospital and Harvard Medical School, Boston, Massachusetts, United States of America

*syip@lroc.harvard.edu

☯ These authors contributed equally to this work.

Citation: Yip S, McCall K, Aristophanous M, Chen AB, Aerts HJWL, et al. (2014) Comparison of Texture Features Derived from Static and Respiratory-Gated PET Images in Non-Small Cell Lung Cancer. PLoS ONE 9(12): e115510. doi:10.1371/journal.pone.0115510

Editor: Olga Y. Gorlova, Geisel School of Medicine at Dartmouth College, United States of America

Received: July 3, 2014

Accepted: November 24, 2014

Published: December 17, 2014

Data Availability: The authors confirm that, for approved reasons, some access restrictions apply to the data underlying the findings. Ethical restrictions prevent data from being publicly shared. Data are available from the Dana-Farber Cancer Institute Institutional Data Access for researchers who meet the criteria for access to confidential data. Requests for data may be sent to Dr. Aileen Chen at achen@lroc.harvard.edu.

Funding: The authors have no support or funding to report.

Competing Interests: The authors have declared that no competing interests exist.

Abstract

Background: PET-based texture features have been used to quantify tumor heterogeneity due to their predictive power in treatment outcome. We investigated the sensitivity of texture features to tumor motion by comparing static (3D) and respiratory-gated (4D) PET imaging.

Methods: Twenty-six patients (34 lesions) received 3D and 4D [^{18}F]FDG-PET scans before the chemo-radiotherapy. The acquired 4D data were retrospectively binned into five breathing phases to create the 4D image sequence. Texture features, including Maximal correlation coefficient (MCC), Long run low gray (LRLG), Coarseness, Contrast, and Busyness, were computed within the physician-defined tumor volume. The relative difference ($\delta_{3D\text{-}4D}$) in each texture between the 3D- and 4D-PET imaging was calculated. Coefficient of variation (CV) was used to determine the variability in the textures between all 4D-PET phases. Correlations between tumor volume, motion amplitude, and $\delta_{3D\text{-}4D}$ were also assessed.

Results: 4D-PET increased LRLG (=1%–2%, $p<0.02$), Busyness (=7%–19%, $p<0.01$), and decreased MCC (=1%–2%, $p<7.5\times10^{-3}$), Coarseness (=5%–10%, $p<0.05$) and Contrast (=4%–6%, $p>0.08$) compared to 3D-PET. Nearly negligible variability was found between the 4D phase bins with CV<5% for MCC, LRLG, and Coarseness. For Contrast and Busyness, moderate variability was found with CV=9% and 10%, respectively. No strong correlation was found between the tumor

volume and $\delta_{3D\text{-}4D}$ for the texture features. Motion amplitude had moderate impact on δ for MCC and Busyness and no impact for LRLG, Coarseness, and Contrast. ***Conclusions:*** Significant differences were found in MCC, LRLG, Coarseness, and Busyness between 3D and 4D PET imaging. The variability between phase bins for MCC, LRLG, and Coarseness was negligible, suggesting that similar quantification can be obtained from all phases. Texture features, blurred out by respiratory motion during 3D-PET acquisition, can be better resolved by 4D-PET imaging. 4D-PET textures may have better prognostic value as they are less susceptible to tumor motion.

Introduction

Positron emission tomography (PET) with [^{18}F]fluorodeoxyglucose (FDG), a surrogate of glucose metabolism, is an essential clinical tool for tumor diagnosis, staging, and monitoring tumor progression [1–4]. Accurate quantification of tumor characteristics based on [^{18}F]FDG-PET images can provide valuable information for optimizing therapy [5, 6]. Standardized uptake value (SUV) measures such as maximum, peak, mean, and total SUV, are commonly used for quantification of the tumor characteristics [7–10]. High baseline SUV uptake has been found to be associated with poor treatment outcome in many tumors, such as esophageal, lung, and head-and-neck cancer [11–13].

High intra-tumoral heterogeneity has been shown to relate to poor prognosis and treatment resistance [14, 15]. However, SUV measures fail to adequately capture the spatial heterogeneity of the intra-tumoral uptake distribution [16, 17]. Therefore, texture features, which can be derived from a number of mathematical models of the relationship between multiple voxels and their neighborhood, are proposed to describe tumor heterogeneity [18, 19]. Particularly, pretreatment [^{18}F]FDG PET texture features have shown promise for delineating nodal and tumor volumes [20, 21] and assessing therapeutic response [22–24]. Studies have suggested that texture features perform better than SUV measures in treatment outcome prediction [22, 24–26]. For example, Cook *et al* (2013) compared the predictive power of common SUV measures and four neighborhood gray-tone difference matrix (NGTDM) derived textures in non-small cell lung cancer (NSCLC) patients [27]. They found that NGTDM-derived Coarseness, Contrast, and Busyness were not only better prognostic predictors than the SUV measures, but also better able to differentiate responders from nonresponders.

Despite the clinical potential of texture features, the accurate quantification of texture features may be hindered by respiratory motion in lung cancer patients. Motion induced image blurring in static PET images (3D PET) can lead to reduction in tumor uptake and over estimation of metabolic tumor volume [28–30]. 4D PET imaging gates PET image acquisition with respiratory motion in order to improve PET image quality and has been shown to reduce motion

blurring in the PET images, providing more accurate quantification of lung tumor activity [28, 31–34]. We hypothesize that fine texture features are likely to be blurred during 3D PET acquisition of lung tumors.

With the growing interest of texture features and tumor heterogeneity, the impact of tumor motion on PET-based quantification needs to be studied as it is still yet unknown. In this study, we compared the quantification of texture features between 3D and 4D PET imaging. Although numerous texture features can be found in the literature [22, 35, 36], we focused on five texture features. Particularly, three NGTDM derived Coarseness, Contrast, and Busyness due to their predictive value in lung cancer patients [27]. A gray level co-occurrence matrix (GLCM) derived Maximal Correlation Coefficient (MCC) [37] and gray level run length matrix (GLRLM) derived Long Run Low Gray level emphasis (LRLG) [38] were also computed due to their robustness against variation of reconstruction parameters of PET images [36].

The NGTDM texture features were originally designed to resemble human perception and were first proposed by Amadasun and King (1989) [18]. In a coarse image, the texture is made up by large patterns, such as large area with uniform intensity distribution. Contrast measures the intensity difference between neighboring regions within the tumor. Busyness is a measure of the intensity change between multiple voxels and their surroundings. GLCM-MCC was first introduced by Haralick *et al* in 1973 [37] and is used to measure the statistical relationship between two neighboring voxels. GLRLM-LRLG measures the joint distribution of long runs and low intensity values, where a run is the distance between two consecutive voxels with the same intensity in a specific direction [38].

Methods

Patients and imaging

This study was conducted under the Dana-Farber Cancer Institute institutional review board (IRB) approved protocol (protocol #: 06-294) and written consents were obtained from all patients. Twenty-six patients (mean age $=65\pm10$ yr, 14 males, 12 females) with NSCLC received a treatment planning CT (both 3D and 4D) two weeks before the start of radiotherapy with or without concurrent chemotherapy. 3D [^{18}F]FDG-PET/CT, a free breathing chest CT, and a 4D [^{18}F]FDG-PET scans were acquired 1–2 weeks prior to the therapy. There were sixteen patients with adenocarcinoma and ten patients with squamous cell carcinoma. The internal tumor volumes (ITV), which encompassed tumor motion, of thirty-four lesions (1–3 malignant tumors/patient) were delineated by an experienced radiation oncologist on a 4D planning CT. 3D PET and 4D PET scans were performed on a Siemens Biograph PET/CT scanner (Siemens AG, Erlangen, Germany). Attenuation correction of 3D PET images was performed using the whole body 3D CT images, while 4D PET images were corrected by the free breathing chest CT images. 3D PET scans were acquired approximately

100 min after injection of 16.7–22mCi of [^{18}F]FDG in the patients. For the 3D PET scan, the images were acquired for 3–5 min/bed position in six to seven bed positions. The 3D PET images were reconstructed with ordered-subset expectation-maximization (OSEM) with 4 iterations, 8 subsets, 7 mm full-width-half-maximum (FWHM) post-filtration, and sampled onto a 168×168 grid comprised of 4.06×4.06 mm^2 pixel. The image acquisition of 4D PET followed immediately after the completion of the 3D PET scan.

4D PET images were acquired at one bed position centered on the tumor and covering part of the lung for 20–30 min, depending on the comfort of the patients. An AZ-733V respiratory gating system (Anzai Medical System, Tokyo, Japan) was employed to monitor patient respiratory motion [39]. The acquired data were retrospectively binned into five phases starting at inhale peak (bin 1) to create the 4D image sequence using the phase-based algorithm provided by the Siemens Biograph PET/CT scanner (Siemens AG, Erlangen, Germany). In particular, the five phase bins, corresponded to the end of inhalation (bin 1), inhalation–to–exhalation (bin 2), mid exhalation (bin 3), end of exhalation (bin4), exhalation–to inhalation (bin 5), respectively. The respiratory gated 4D PET images were reconstructed with OSEM with 2 iterations, 8 subsets, 5 mm FWHM, and sampled onto a 256×256 grid comprised of 2.67×2.67 mm^2 pixel.

Texture features

Planning CT was rigidly registered to 3D- and 4D-PET images with normalized mutual information. The transformations were then applied to each ITV. The 3D and 4D PET images were cropped using the registered ITV contour to crop out the tumor region. Number of voxels per tumor region ranged from 85 to 6483 with median number of voxels=545. Prior to texture feature computation, all PET images ($PET(\vec{x})$) were preprocessed using the following equation,

$$PET'(\vec{x}) = 32 \cdot \frac{PET(\vec{x}) - \min PET}{\max PET - \min PET} \quad (1)$$

Where minPET and maxPET are the maximum and minimum intensities of PET within the tumor region. The intensity range of the post-processed image ($PET'(\vec{x})$) was converted into 32 discrete values as suggested by Orlhac *et al* (2014) [40].

Within the tumor region, the following four neighborhood gray-tone difference matrix (NGTDM) derived texture features were computed to quantify tumor heterogeneity: Coarseness, Contrast, Busyness, and Complexity. These were implemented in MATLAB (The Mathworks Inc. Natrick MA) using the Chang-Gung Image Texture Analysis Toolbox [41, 42]. The mathematical definitions of the NGTDM, GLCM, and GLRLM texture features can be found in Amadasun and King (1989) [18], Haralick *et al* (1973, 1979) [37, 43], and Galloway (1975) [38], respectively.

3D (168×168) and 4D (256×256) PET images were reconstructed to different matrix sizes based on different reconstruction parameters. Additionally, due to the

difference in 3D and 4D PET imaging acquisition times, fewer photon counts and higher noise may be found in the 4D PET images. Therefore, all 4D PET images were downsampled to the same grid/resolution of 3D PET images using linear interpolation prior to texture feature computation to reduce noise.

Data analysis

The relative difference ($\delta_{3D\text{-}4D}$) in texture features between 3D and 4D PET were calculated:

$$\delta_{3D-4D} = 100 \cdot \frac{Q_j^{4D} - Q^{3D}}{Q^{3D}} \tag{2}$$

Where Q^{3D} is the quantification (i.e. texture features measures) based on 3D PET, Q_j^{4D} is the quantification based on bin j of the 4D PET images. Wilcoxon signed-rank test ($p<0.05$) was performed on pairs to determine if Q^{3D} and Q_j^{4D} were significantly different. We calculated an avid tumor volume (ATV) as thresholded PET images with SUV over 40% maximum SUV within the ITV [29]. We investigated the influence of ATV and ITV on $\delta_{3D\text{-}4D}$ using Spearman's correlation coefficient (R) with significant value of $p=0.05$.

Kruskal-Wallis test was used to assess if one phase was significantly different from the other phases ($p<0.05$). The variability in the texture features measures between all five phase bins was assessed using the coefficient of variation (CV).

$$CV = \frac{\sqrt{\frac{1}{5-1} \cdot \sum_{bin=1}^{5} (Q_{bin}^{4D} - \bar{Q}^{4D})^2}}{\bar{Q}^{4D}} \tag{3}$$

$$\bar{Q}^{4D} = \frac{1}{5} \cdot \sum_{bin=1}^{5} Q_{bin}^{4D} \tag{4}$$

To estimate the extent of motion, the centers of mass ($\vec{C}_j$) of the PET avid region (ATV) on all five 4D PET bins were recorded. The amplitude of the tumor motion was estimated using the maximum difference in $\vec{C}_j$ between the five bins [28, 29]

$$Amp = \max\{|\vec{C}_i - \vec{C}_j|\} \tag{5}$$

Where i and j range from 1 to 5.

To study the impact of tumor motion, we calculated the Spearman's correlation coefficient for Amplitude:ATV ratio and $\delta_{3D\text{-}4D}$ with significant value $p=0.05$. Amplitude:ATV ratio is a measure of motion amplitude relative to the tumor volume. Large Amplitude:ATV ratio indicates large tumor movement relative to the tumor size.

Furthermore, textures may be affected by motion differently according to the tumor histology. Therefore, we investigated if $\delta_{3D\text{-}4D}$ were significantly different between adenocarcinomas (21 lesions) and squamous cell carcinomas (13 lesions) using Mann-Whitney U-test with $p<0.05$.

Results

4D PET images appeared to have higher uptake and less blurring than the corresponding 3D PET images (Fig. 1). The differences between 3D and 4D PET were found to be significant ($p<<0.01$) for Busyness, MCC, and LRLG as shown in Table 1. Significant difference for Coarseness was found in all bins ($p<<0.01$) except in bin 2 ($p=0.59$) (Table 1). The Coarseness determined on the 3D PET images was about 10% higher than the 4D PET. 4D PET images were found to have as much as a 19% increase in Busyness, compared to the corresponding 3D PET images (Table 1, Fig. 2). MCC was found to be 2% higher in 3D PET than 4D PET, while 2% higher LRLG was found in 4D PET when comparing to 3D PET. However, Contrast on 3D images was only about 5% lower when compared to 4D PET and $\delta_{3D\text{-}4D}$ was not significant ($p>0.08$) (Table 1, Fig. 2).

None of the phases were significantly different from the other for any texture features ($p>0.90$, Kruskal-Wallis test). Negligible to moderate variability in the texture features was found between the five phase bins (Fig. 2). CV was only 1% for MCC and LRLG, 5% for Coarseness, 9% and 10% for Contrast and Busyness, respectively. The avid tumor volume (ATV) was poorly correlated to $\delta_{3D\text{-}4D}$ for all texture features ($R=-0.24$–0.38, $p=0.03$–0.07). The correlation between internal tumor volumes (ITV) and $\delta_{3D\text{-}4D}$ were also found to be poor for all textures ($R=-0.31$–0.30, $p>0.02$), except LGLR. Although $\delta_{3D\text{-}4D}$ for LGLR was moderately influenced by ITV ($R=-0.62$–-0.31, $p=8.3\times10^{-5}$–0.08), the average $\delta_{3D\text{-}4D}<2\%$.

Average motion amplitude was found to be 4.4 ± 4.6 mm (0.6–20.5 mm). As shown in Table 2, moderate to substantial correlation was found between Amplitude:ATV (mm^{-2}) and $\delta_{3D\text{-}4D}$ for Busyness ($R=0.38$–0.54) and MCC ($R=-0.70$–-0.41) in bin 3–5, whereas poor correlation was found in bin 1–2 with $R=-0.03$–0.12. The correlations were also poor for Coarseness ($R=-0.32$–0.18), Contrast ($R=-0.35$–-0.10), and LRLG ($R=0.08$–0.34) (Table 2). Moreover, $\delta_{3D\text{-}4D}$ were not significantly different between the histologies, adenocarcinomas and squamous cell carcinomas, with $p>0.26$ (Table 3).

Discussion

In this study, we investigated the sensitivity of prognostic PET texture features to respiratory motion. Our results suggest that texture measures are sensitive to tumor motion. Substantial differences between 3D and 4D ($\delta_{3D\text{-}4D}>10\%$) were found in Coarseness and Busyness. Therefore, the temporal resolution offered by 4D PET imaging may lead to more accurate quantification of image features.

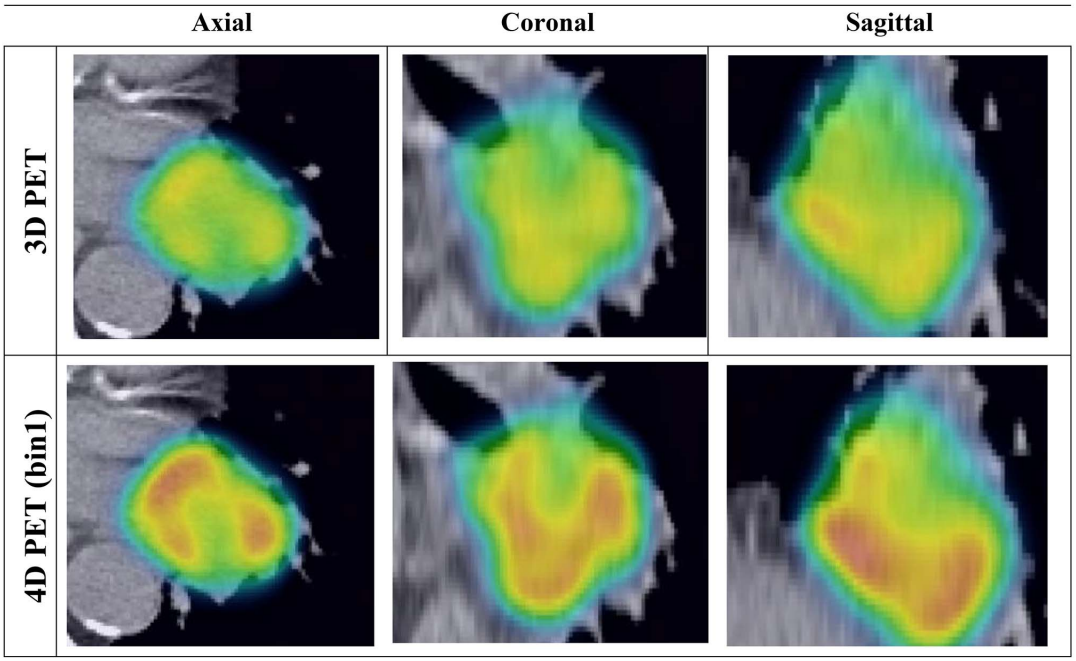

Fig. 1. 3D (top row) and 4D (bottom row) PET images overlaid onto the 3D CT. All images are displayed in the same intensity window with SUV between 1 and 15.

doi:10.1371/journal.pone.0115510.g001

Table 1. The mean difference ($\delta_{3D\text{-}4D}$) between 3D and 4D PET images in texture features.

	Bin-1	Bin-2	Bin-3	Bin-4	Bin-5
MCC	$-1\pm2\%$	$-1\pm3\%$	$-3\pm2\%$	$-3\pm3\%$	$-2\pm3\%$
	(−6%–7%)	(−11%–8%)	(−11%–0%)	(−13%–2%)	(−11%–6%)
	$p=2.0\times10^{-4}$	$p=7.5\times10^{-3}$	$p=6.2\times10^{-7}$	$p=3.8\times10^{-6}$	$p=1.4\times10^{-4}$
LRLG	$2\pm3\%$	$1\pm2\%$	$1\pm2\%$	$1\pm3\%$	$1\pm3\%$
	(−4%–15%)	(−5%–5%)	(−7%–5%)	(−9%–9%)	(−12%–8%)
	$p=1.5\times10^{-3}$	$p=2.4\times10^{-3}$	$p=0.02$	$p=9.6\times10^{-3}$	$p=8.3\times10^{-3}$
Coarseness	$-7\pm8\%$	$-5\pm10\%$	$-9\pm9\%$	$-11\pm8\%$	$-6\pm10\%$
	(−30%–16%)	(−30%–15%)	(−31%–7%)	(−30%–4%)	(−21%–23%)
	$p=4.1\times10^{-4}$	$p=0.05$	$p=1.1\times10^{-4}$	$p=1.0\times10^{-4}$	$p=2.3\times10^{-3}$
Contrast	$5\pm14\%$	$4\pm15\%$	$6\pm22\%$	$5\pm18\%$	$4\pm19\%$
	(−29%–40%)	(−32%–44%)	(−36%–93%)	(−38%–71%)	(−39%–68%)
	$p=0.08$	$p=0.72$	$p=0.54$	$p=0.12$	$p=0.55$
Busyness	$8\pm16\%$	$7\pm18\%$	$13\pm18\%$	$19\pm24\%$	$9\pm18\%$
	(−25%–63%)	(−30%–52%)	(−20%–67%)	(−15%–85%)	(−36%–55%)
	$p=1.4\times10^{-3}$	$p=0.01$	$p=1.3\times10^{-4}$	$p=3.0\times10^{-5}$	$p=7.3\times10^{-4}$

The ranges of $\delta_{3D\text{-}4D}$ and the p-values for Wilcoson signed-rank test are also shown. MCC=maximal correlation coefficient. LRLG=Long run low gray-level emphasis

doi:10.1371/journal.pone.0115510.t001

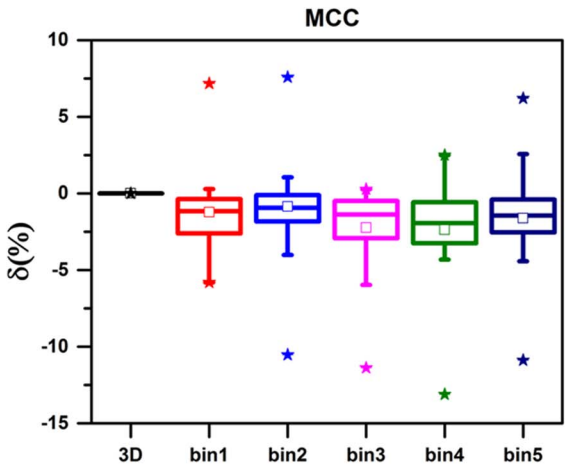
MCC
δ(%)
10
5
0
-5
-10
-15
3D
bin1
bin2
bin3
bin4
bin5

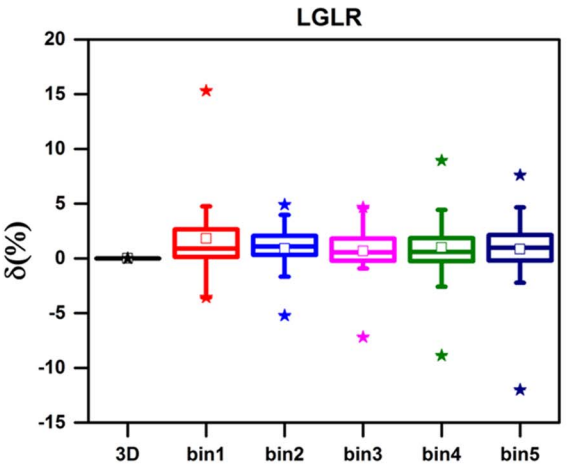
LGLR
δ(%)
20
15
10
5
0
-5
-10
-15
3D
bin1
bin2
bin3
bin4
bin5

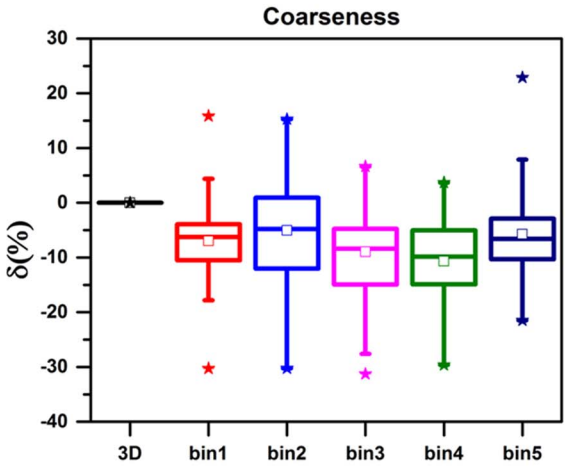
Coarseness
δ(%)
30
20
10
0
-10
-20
-30
-40
3D
bin1
bin2
bin3
bin4
bin5

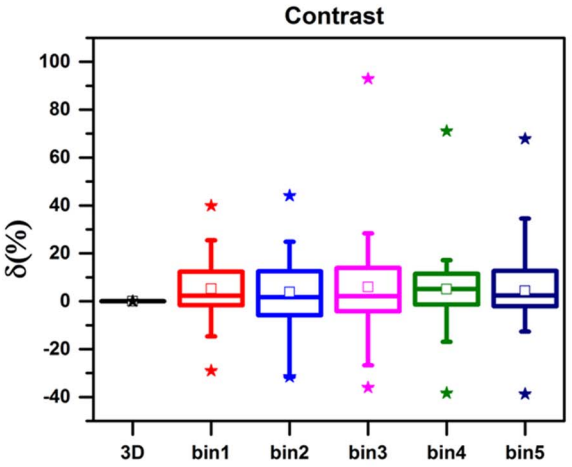
Contrast
δ(%)
100
80
60
40
20
0
-20
-40
3D
bin1
bin2
bin3
bin4
bin5

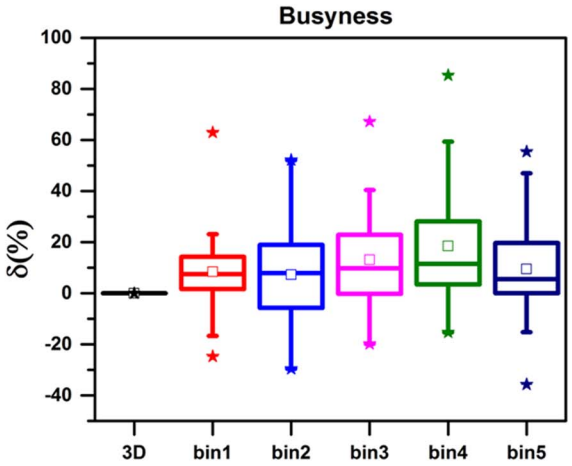
Busyness
δ(%)
100
80
60
40
20
0
-20
-40
3D
bin1
bin2
bin3
bin4
bin5

Fig. 2. Distribution of the difference between 3D and 4D PET ($\delta_{3D\text{-}4D}$) in the texture features across 34 lesions. The top vertical line of a boxplot represents 75th—95th percentiles of the data. The bottom vertical line is the 5th—25th percentiles. Interquartile range (IQR) of the data is indicated by the width of the boxplot. Asterisks indicate the maximum and minimum differences. Median and mean differences are indicated by bar and square inside the box plots, respectively. MCC=Maximal correlation coefficient. LRLG=Long run low gray-level emphasis. The first boxplot represents the comparisons of 3D and 3D PET textures ($\delta_{3D\text{-}3D}$). $\delta_{3D\text{-}3D}$ is therefore zero by definition as shown in the first ''boxplot'' for each texture.

doi:10.1371/journal.pone.0115510.g002

Coarseness, Contrast, and Busyness considered in this study were originally designed to resemble human perception and were first proposed by Amadasun and King (1989) [18]. Cook *et al* (2012) [27] have shown that these three texture features are clinically relevant to lung cancer due to their predictive value for patient outcome. In a coarse image, the texture is made up by large patterns, such as large area with uniform intensity distribution. As breathing motion blurs the fine textures in the images, the 3D PET images appear to be more uniform (Fig. 1) and therefore have more Coarseness than 4D PET images. The sensitivity of Contrast was found to be insignificant to motion induced blurring. The intensity difference between neighboring regions within the tumor was observed to be more pronounced in 4D PET image (Fig. 1), leading to slightly higher ($\delta_{3D\text{-}4D}$~5%) Contrast in 4D PET than 3D PET images. Busyness is a measure of the intensity change between single voxels and their surroundings. Busyness computed with 4D PET images was found to be as much as 20% higher than the 3D PET images. Since $\delta_{3D\text{-}4D}$ tended to be higher at large Amplitude:ATV, the quantification of Busyness is especially sensitive to large relative tumor amplitude. However, 3D PET imaging was employed in the study of Cook *et al* (2012). Our results suggest that the quantification and prognostic value of busyness can be adversely affected by tumor motion.

GLCM-MCC and GLRLM-LRLG were included in the 3D vs 4D PET imaging comparison as they are insensitive to reconstruction parameters of PET images [36]. Tumor motion blurring in 3D PET image can reduce intensity difference between neighboring voxels. Therefore, neighboring voxels are better correlated in

Table 2. Spearman correlation coefficient of Amplitude:ATV (mm^{-2}) and $\delta_{3D\text{-}4D}$ and its p-value.

	Bin-1	Bin-2	Bin-3	Bin-4	Bin-5
MCC	−0.07	0.12	*−0.70*	*−0.62*	*−0.41*
	p=0.71	p=0.51	*$p=4.3\times10^{-6}$*	*$p=1.1\times10^{-4}$*	*p=0.02*
LRLG	*0.34*	0.27	0.08	0.24	0.19
	p=0.05	p=0.11	p=0.64	p=0.16	p=0.28
Coarseness	0.05	0.18	−0.32	−0.23	0.06
	p=0.78	p=0.31	p=0.07	p=0.19	p=0.74
Contrast	−0.14	−0.20	−0.10	−0.23	−0.35
	p=0.44	p=0.26	p=0.59	p=0.18	p=0.04
Busyness	0.00	−0.03	*0.43*	*0.54*	*0.38*
	p=0.99	p=0.88	*p=0.01*	*$p=9.3\times10^{-4}$*	*p=0.03*

MCC=Maximal correlation coefficient. LRLG=Long run low gray-level emphasis.

doi:10.1371/journal.pone.0115510.t002

Table 3. p-values for the comparison of $\delta_{3D\text{-}4D}$ between adenocarcinoma and squamous cell carcinoma using Mann-Whitney U-test.

	Bin-1	Bin-2	Bin-3	Bin-4	Bin-5
MCC	p=0.48	p=0.77	p=0.53	p=0.90	p=0.84
LRLG	p=0.77	p=0.26	p=0.48	p=0.30	p=0.49
Coarseness	p=0.87	p=0.61	p=0.79	p=0.55	p=0.55
Contrast	p=0.46	p=0.68	p=1.00	p=0.66	p=0.45
Busyness	p=0.59	p=0.80	p=0.93	p=0.86	p=0.78

doi:10.1371/journal.pone.0115510.t003

3D PET than 4D PET, leading to significant 2% higher MCC in 3D PET images. LRLG measures the joint probability of long runs and low gray values. As observed in Fig. 1, low intensity voxels are more localized (less distance apart) in the motion blurred 3D PET than in the 4D PET images. Therefore, LRLG was higher in 4D PET than 3D PET.

In this study, the 4D PET images were binned into five phases. The activity uptake of each bin was slightly different as in Huang and Wang (2013) [30]. The bin with the highest SUV_{max} is often chosen to be the "best" bin for 4D PET image [29, 44, 45]. However, we found that the variability between phase bins for MCC, LRLG, and Coarseness were negligible (CV$<$5%), suggesting that similar quantification can be obtained from all phases. The small variability may be due to the small tumor amplitude (4.4 ± 4.6 mm) in our dataset. On the other hand, the phase bin variability was found to be moderate for Contrast and Busyness (CV$\sim$10%). The values of Contrast and Busyness may depend on the choice of phase-bin. MCC, LRLG, and Coarseness are independent of the choice of phase-bin, and therefore should be recommended for quantification of tumor characteristics in 4D PET imaging.

Apart from the texture features, studies often investigate the effect of respiratory motion on the quantification of various SUV measures, especially the maximum SUV [28, 29, 33]. The SUV_{max} was found to increase with 4D PET imaging from 25% to 80% in these studies. The motion induced artifacts not only lower maximum tumor uptake on the 3D PET images, but may also lead to misclassification of lesions. For example, García Vicente *et al* (2010) compared the SUV_{max} determined on 3D and 4D PET images for 42 lesions in lung cancer patients [33]. Tumor with SUV_{max} over 2.5 was considered malignant in their study. As a result, 40% (17/42) of the lesions needed to be changed from benign to malignant. To this end, although the results are not shown, we also compared the differences in four SUV measures (SUV_{max}, SUV_{peak}, SUV_{mean}, and SUV_{total}). 4D PET imaging increased the measurements of SUV_{max} and SUV_{peak} by about 30% and 25%, respectively, while increased for SUV_{mean} and SUV_{total} were only about 5%. Our results in SUV_{max} are comparable to the previous studies [28, 29, 33].

However, there is one limitation of our textures and SUV comparison as it has been shown that malignant tumor tissue can continuously increase the uptake of [^{18}F]FDG even 2 hours after injection [46–48]. While the 3D PET imaging was

acquired about 100 min after the [^{18}F]FDG-PET injection, 4D PET imaging was acquired between 118–135 min after injection. Therefore, the increase in [^{18}F]FDG-PET seen in our study may not be due solely to respiratory motion. Dong *et al* (2013) found a significant correlation between SUV_{max} and textures (entropy and energy) derived from PET intensity histograms in patients with esophageal cancer [49]. SUV_{max} was also found to be highly correlated to entropy and energy in a study conducted by Orlhac *et al* (2014) [40] using patients with metastatic colorectal, lung, and breast cancer. These two studies may therefore suggest that the histogram derived textures are likely to be affected by the delayed imaging. However, none of the textures that were used in our study has been found to be highly correlated with SUV_{max} [40]. This may be due to the fact that the textures we used are based on the spatial relationship between neighborhoods of voxels, and are not directly dependent on the intensity value of single or multiple voxels within the tumors. However, further study is needed to better understand the impact of delayed imaging on texture quantification.

All the PET images in our study underwent attenuation correction using the free breathing CT images. The blurred anatomical mismatched of the PET/CT scans due to respiratory motion may affect the quality of the attenuation corrected 4D PET images, and subsequently the quantification of texture features [29, 50, 51]. Moreover, due to the difference in 3D and 4D PET imaging acquisition times, fewer photon counts and higher noise may be found in 4D PET images, which may subsequently affect the accuracy of texture feature definition. To mitigate the effect of noise, all 4D PET images have a minimum acquisition time of 20 min. These potential effects will be explored further in a future study.

Conclusions

Texture features, representing tumor heterogeneity, are blurred out by respiratory motion during 3D PET acquisition. 4D PET imaging reduces motion blurring, enabling PET-based features to be better resolved. Significant differences were found in MCC, LRLG, Coarseness, and Busyness between 3D and 4D PET imaging. When measuring tumor heterogeneity characteristics with PET imaging, reduced motion blurring by 4D PET acquisition enables significantly better spatial resolution of texture features. 3D PET textures may lead to inaccurate prediction of treatment outcome, hindering optimal lung cancer patient management. 4D PET textures may have better prognostic value as they are less susceptible to tumor motion.

Author Contributions

Conceived and designed the experiments: SY KM MA AC HA RB. Performed the experiments: SY KM HA RB. Analyzed the data: SY KM HA RB. Contributed reagents/materials/analysis tools: SY KM MA AC HA RB. Wrote the paper: SY RB.

References

1. **Vansteenkiste JF, Stroobants SG, Dupont PJ, De Leyn PR, Verbeken EK, et al.** (1999) Prognostic Importance of the Standardized Uptake Value on 18F-Fluoro-2-Deoxy-Glucose–Positron Emission Tomography Scan in Non–Small-Cell Lung Cancer: An Analysis of 125 Cases. Journal of Clinical Oncology 17: 3201–3206.
2. **Phelps ME** (2000) Positron emission tomography provides molecular imaging of biological processes. Proceedings of the National Academy of Sciences 97: 9226–9233.
3. **Lin P, Koh E-S, Lin M, Vinod SK, Ho-Shon I, et al.** (2011) Diagnostic and staging impact of radiotherapy planning FDG-PET-CT in non-small-cell lung cancer. Radiotherapy and Oncology 101: 284–290.
4. **Weber WA, Petersen V, Schmidt B, Tyndale-Hines L, Link T, et al.** (2003) Positron Emission Tomography in Non–Small-Cell Lung Cancer: Prediction of Response to Chemotherapy by Quantitative Assessment of Glucose Use. Journal of Clinical Oncology 21: 2651–2657.
5. **de Geus-Oei L-F, Vriens D, van Laarhoven HWM, van der Graaf WTA, Oyen WJG** (2009) Monitoring and Predicting Response to Therapy with 18F-FDG PET in Colorectal Cancer: A Systematic Review. Journal of Nuclear Medicine 50: 43S–54S.
6. **MacManus M, Nestle U, Rosenzweig KE, Carrio I, Messa C, et al.** (2009) Use of PET and PET/CT for Radiation Therapy Planning: IAEA expert report 2006–2007. Radiotherapy and Oncology 91: 85–94.
7. **Erasmus JJ, Rohren E, Swisher SG** (2009) Prognosis and Reevaluation of Lung Cancer by Positron Emission Tomography Imaging. Proceedings of the American Thoracic Society 6: 171–179.
8. **Wahl RL, Jacene H, Kasamon Y, Lodge MA** (2009) From RECIST to PERCIST: Evolving Considerations for PET Response Criteria in Solid Tumors. Journal of Nuclear Medicine 50: 122S–150S.
9. **Pandit N, Gonen M, Krug L, Larson S** (2003) Prognostic value of [18F]FDG-PET imaging in small cell lung cancer. European Journal of Nuclear Medicine and Molecular Imaging 30: 78–84.
10. **Usmanij EA, Geus-Oei L-Fd, Troost EGC, Peters-Bax L, van der Heijden EHFM, et al.** (2013) 18F-FDG PET Early Response Evaluation of Locally Advanced Non–Small Cell Lung Cancer Treated with Concomitant Chemoradiotherapy. Journal of Nuclear Medicine 54: 1528–1534.
11. **Zhang H-q, Yu J-m, Meng X, Yue J-b, Feng R, et al.** (2011) Prognostic value of serial [18F]fluorodeoxyglucose PET-CT uptake in stage III patients with non-small cell lung cancer treated by concurrent chemoradiotherapy. European Journal of Radiology 77: 92–96.
12. **Higgins KA, Hoang JK, Roach MC, Chino J, Yoo DS, et al.** (2012) Analysis of Pretreatment FDG-PET SUV Parameters in Head-and-Neck Cancer: Tumor SUVmean Has Superior Prognostic Value. International Journal of Radiation Oncology*Biology*Physics 82: 548–553.
13. **Rizk N, Downey RJ, Akhurst T, Gonen M, Bains MS, et al.** (2006) Preoperative 18[F]-Fluorodeoxyglucose Positron Emission Tomography Standardized Uptake Values Predict Survival After Esophageal Adenocarcinoma Resection. The Annals of Thoracic Surgery 81: 1076–1081.
14. **Gerlinger M, Rowan AJ, Horswell S, Larkin J, Endesfelder D, et al.** (2012) Intratumor Heterogeneity and Branched Evolution Revealed by Multiregion Sequencing. New England Journal of Medicine 366: 883–892.
15. **Chicklore S, Goh V, Siddique M, Roy A, Marsden P, et al.** (2013) Quantifying tumour heterogeneity in 18F-FDG PET/CT imaging by texture analysis. European Journal of Nuclear Medicine and Molecular Imaging 40: 133–140.
16. **van Velden F, Cheebsumon P, Yaqub M, Smit E, Hoekstra O, et al.** (2011) Evaluation of a cumulative SUV-volume histogram method for parameterizing heterogeneous intratumoural FDG uptake in non-small cell lung cancer PET studies. Eur J Nucl Med Mol Imaging 38: 1636–1647.
17. **Cheng N-M, Fang Y-H, Yen T-C** (2013) The promise and limits of PET texture analysis. Annals of Nuclear Medicine 27: 867–869.
18. **Amadasun M, King R** (1989) Textural features corresponding to textural properties. Systems, Man and Cybernetics, IEEE Transactions on 19: 1264–1274.
19. **Castellano G, Bonilha L, Li LM, Cendes F** (2004) Texture analysis of medical images. Clinical Radiology 59: 1061–1069.

20. **Yu H, Caldwell C, Mah K, Poon I, Balogh J, et al.** (2009) Automated Radiation Targeting in Head-and-Neck Cancer Using Region-Based Texture Analysis of PET and CT Images. International Journal of Radiation Oncology*Biology*Physics 75: 618–625.

21. **Huan Y, Caldwell C, Mah K, Mozeg D** (2009) Coregistered FDG PET/CT-Based Textural Characterization of Head and Neck Cancer for Radiation Treatment Planning. Medical Imaging, IEEE Transactions on 28: 374–383.

22. **El Naqa I, Grigsby PW, Apte A, Kidd E, Donnelly E, et al.** (2009) Exploring feature-based approaches in PET images for predicting cancer treatment outcomes. Pattern Recognition 42: 1162–1171.

23. **Tixier F, Hatt M, Le Rest CC, Le Pogam A, Corcos L, et al.** (2012) Reproducibility of Tumor Uptake Heterogeneity Characterization Through Textural Feature Analysis in 18F-FDG PET. Journal of Nuclear Medicine 53: 693–700.

24. **Tixier F, Le Rest CC, Hatt M, Albarghach N, Pradier O, et al.** (2011) Intratumor Heterogeneity Characterized by Textural Features on Baseline 18F-FDG PET Images Predicts Response to Concomitant Radiochemotherapy in Esophageal Cancer. Journal of Nuclear Medicine 52: 369–378.

25. **Yang F, Thomas M, Dehdashti F, Grigsby P** (2013) Temporal analysis of intratumoral metabolic heterogeneity characterized by textural features in cervical cancer. European Journal of Nuclear Medicine and Molecular Imaging 40: 716–727.

26. **Eary JF, O'Sullivan F, O'Sullivan J, Conrad EU** (2008) Spatial Heterogeneity in Sarcoma 18F-FDG Uptake as a Predictor of Patient Outcome. Journal of Nuclear Medicine 49: 1973–1979.

27. **Cook GJR, Yip C, Siddique M, Goh V, Chicklore S, et al.** (2013) Are Pretreatment 18F-FDG PET Tumor Textural Features in Non–Small Cell Lung Cancer Associated with Response and Survival After Chemoradiotherapy? Journal of Nuclear Medicine 54: 19–26.

28. **Nehmeh SA, Erdi YE, Ling CC, Rosenzweig KE, Schoder H, et al.** (2002) Effect of Respiratory Gating on Quantifying PET Images of Lung Cancer. Journal of Nuclear Medicine 43: 876–881.

29. **Aristophanous M, Yong Y, Yap JT, Killoran JH, Allen AM, et al.** (2012) Evaluating FDG uptake changes between pre and post therapy respiratory gated PET scans. Radiotherapy and Oncology 102: 377–382.

30. **Huang T-C, Wang Y-C** (2013) Deformation Effect on SUVmax Changes in Thoracic Tumors Using 4-D PET/CT Scan. PLoS ONE 8: e58886.

31. **Lupi A, Zaroccolo M, Salgarello M, Malfatti V, Zanco P** (2009) The effect of 18F-FDG-PET/CT respiratory gating on detected metabolic activity in lung lesions. Annals of Nuclear Medicine 23: 191–196.

32. **Werner MK, Parker JA, Kolodny GM, English JR, Palmer MR** (2009) Respiratory Gating Enhances Imaging of Pulmonary Nodules and Measurement of Tracer Uptake in FDG PET/CT. American Journal of Roentgenology 193: 1640–1645.

33. **García Vicente AM, Soriano Castrejón AM, Talavera Rubio MP, León Martín AA, Palomar Muñoz AM, et al.** (2010) 18F-FDG PET-CT respiratory gating in characterization of pulmonary lesions: approximation towards clinical indications. Annals of Nuclear Medicine 24: 207–214.

34. **Didierlaurent D, Ribes S, Batatia H, Jaudet C, Dierickx LO, et al.** (2012) The retrospective binning method improves the consistency of phase binning in respiratory-gated PET/CT. Physics in Medicine and Biology 57: 7829.

35. **Leijenaar RTH, Carvalho S, Velazquez ER, van Elmpt WJC, Parmar C, et al.** (2013) Stability of FDG-PET Radiomics features: An integrated analysis of test-retest and inter-observer variability. Acta Oncologica 52: 1391–1397.

36. **Galavis PE, Hollensen C, Jallow N, Paliwal B, Jeraj R** (2010) Variability of textural features in FDG PET images due to different acquisition modes and reconstruction parameters. Acta Oncologica 49: 1012–1016.

37. **Haralick RM, Shanmugam K, Dinstein IH** (1973) Textural Features for Image Classification. Systems, Man and Cybernetics, IEEE Transactions on SMC-3: 610–621.

38. **Galloway MM** (1975) Texture analysis using gray level run lengths. Computer Graphics and Image Processing 4: 172–179.

39. **Li XA, Stepaniak C, Gore E** (2006) Technical and dosimetric aspects of respiratory gating using a pressure-sensor motion monitoring system. Medical Physics 33: 145–154.

40. **Orlhac F, Soussan M, Maisonobe J-A, Garcia CA, Vanderlinden B, et al.** (2014) Tumor Texture Analysis in 18F-FDG PET: Relationships Between Texture Parameters, Histogram Indices, Standardized Uptake Values, Metabolic Volumes, and Total Lesion Glycolysis. Journal of Nuclear Medicine 55: 414–422.

41. **Cheng N-M, Dean Fang Y-H, Tung-Chieh Chang J, Huang C-G, Tsan D-L, et al.** (2013) Textural Features of Pretreatment 18F-FDG PET/CT Images: Prognostic Significance in Patients with Advanced T-Stage Oropharyngeal Squamous Cell Carcinoma. Journal of Nuclear Medicine 54: 1703–1709.

42. **Fang Y-HD, Lin C-Y, Shih M-J, Wang H-M, Ho T-Y, et al.** (2014) Development and Evaluation of an Open-Source Software Package CGITA; for Quantifying Tumor Heterogeneity with Molecular Images. BioMed Research International 2014: 9.

43. **Haralick RM** (1979) Statistical and structural approaches to texture. Proceedings of the IEEE 67: 786–804.

44. **García Vicente AM, Castrejón AS, León Martín AA, García BG, Pilkington Woll JP, et al.** (2011) Value of 4-Dimensional 18F-FDG PET/CT in the Classification of Pulmonary Lesions. Journal of Nuclear Medicine Technology 39: 91–99.

45. **Guerra L, Ponti E, Elisei F, Bettinardi V, Landoni C, et al.** (2012) Respiratory gated PET/CT in a European multicentre retrospective study: added diagnostic value in detection and characterization of lung lesions. European Journal of Nuclear Medicine and Molecular Imaging 39: 1381–1390.

46. **Cheng G, Torigian D, Zhuang H, Alavi A** (2013) When should we recommend use of dual time-point and delayed time-point imaging techniques in FDG PET? European Journal of Nuclear Medicine and Molecular Imaging 40: 779–787.

47. **Yen R-F, Chen K-C, Lee J-M, Chang Y-C, Wang J, et al.** (2008) 18F-FDG PET for the lymph node staging of non-small cell lung cancer in a tuberculosis-endemic country: Is dual time point imaging worth the effort? European Journal of Nuclear Medicine and Molecular Imaging 35: 1305–1315.

48. **Matthies A, Hickeson M, Cuchiara A, Alavi A** (2002) Dual Time Point 18F-FDG PET for the Evaluation of Pulmonary Nodules. Journal of Nuclear Medicine 43: 871–875.

49. **Dong X, Xing L, Wu P, Fu Z, Wan H, et al.** (2013) Three-dimensional positron emission tomography image texture analysis of esophageal squamous cell carcinoma: relationship between tumor 18F-fluorodeoxyglucose uptake heterogeneity, maximum standardized uptake value, and tumor stage. Nuclear Medicine Communications 34: 40–46

50. **Pan T, Mawlawi O, Nehmeh SA, Erdi YE, Luo D, et al.** (2005) Attenuation Correction of PET Images with Respiration-Averaged CT Images in PET/CT. Journal of Nuclear Medicine 46: 1481–1487.

51. **Park S-J, Ionascu D, Killoran J, Mamede M, Gerbaudo VH, et al.** (2008) Evaluation of the combined effects of target size, respiratory motion and background activity on 3D and 4D PET/CT images. Physics in Medicine and Biology 53: 3661.